

THE NUMERICAL AND EXPERIMENTAL EVALUATION OF A COUPLED BLADE DYNAMIC LIMIT RESPONSE WITH FRICTION CONTACTS

Original

THE NUMERICAL AND EXPERIMENTAL EVALUATION OF A COUPLED BLADE DYNAMIC LIMIT RESPONSE WITH FRICTION CONTACTS / Grant, K., Gastaldi, C., Berruti, T.M., Kellerer, R.. - ELETTRONICO. - 8-B:(2022). (ASME Turbo Expo 2022: Turbomachinery Technical Conference and Exposition, GT 2022 Rotterdam, The Netherlands 2022) [10.1115/GT2022-83393].

Availability:

This version is available at: 11583/2974314 since: 2023-01-03T14:25:17Z

Publisher:

American Society of Mechanical Engineers (ASME)

Published

DOI:10.1115/GT2022-83393

Terms of use:

This article is made available under terms and conditions as specified in the corresponding bibliographic description in the repository

Publisher copyright

ASME postprint/Author's accepted manuscript

(Article begins on next page)

THE NUMERICAL AND EXPERIMENTAL EVALUATION OF A COUPLED BLADE DYNAMIC LIMIT RESPONSE WITH FRICTION CONTACTS

Kelly Grant
Ansaldo Energia
Baden, Switzerland

Chiara Gastaldi
Politecnico di Torino
Turin, Italy

Teresa M. Berruti
Politecnico di Torino
Turin, Italy

Rudolf Kellerer
Ansaldo Energia
Baden, Switzerland

ABSTRACT

Increasing demand on turbine power and efficiency requires larger and higher loaded turbine blades, which in turn requires the consideration of aeromechanical interactions. Whilst CFD tools can reliably predict stability using aerodynamic damping as an indicator, the component of mechanical damping also needs consideration. An understanding of the mechanical damping in the system becomes key to a robust blade design.

Mechanical damping for such a part comes predominantly from friction occurring at the coupling contact faces. It is well established and published that such contact forces are nonlinear in relation to the relative movement at the contact interface. Moreover, contact area, the rigidity in the contact, friction coefficient, and normal contact force must also be considered and included as parameters that influence the result. Consequently, the level of system damping is not a constant, and depends highly on the system response itself, as well as the other forementioned parameters. In the case of self-excited vibration such as flutter, the evaluation of the damped limit response is a part of the blade design process.

A tool has been developed to numerically simulate contact friction forces with the intention of parametrically evaluating the limit response and relating this to the mechanical integrity of the part. This paper presents the modelling of a coupled blade system with friction contact forces, results coming from this evaluation, and a comparison with test data.

Keywords: coupling, blade dynamics, friction, damping

1. INTRODUCTION

New generation turbines respond to the demand of increasing power and efficiency with lighter and higher loaded blades due to fluid-structure interaction [1]. Therefore, understanding and predicting mechanical damping has become a key aspect in blade design. Frictional dissipation using underplatform dampers or through shroud contact faces is well

established as an effective source of mechanical damping in turbine blades. The inclusion of such devices in the blade design has repercussions on the dynamics of the system. In particular, the use of shrouds leads to an increase in the blade's natural frequencies due to the additional constraint imposed at the blade tip. The degree of this constraint can vary significantly in relation to the response amplitudes of the blade itself [2]-[4]. Localized nonlinearities at the contact make the computation of the dynamic response quite complex due to the variable forces transmitted by the friction surfaces, depending on whether the contact surfaces are separated, stuck, or slipping [5]. The resulting nonlinear differential equations of the dynamic response are generally solved by the so-called Multi-Harmonic Balance Method (MHBM) [6]-[12]. The problem is made more complex by the fact that the solution of the nonlinear differential equations in terms of displacement may not be unique. This phenomenon has already been shown in literature [13] and [14] for the case of underplatform dampers. Here, it was shown that the converged frictional forces could vary depending on the initial conditions of the relative displacement set at the contact interface. Thus, providing a non-unique solution and therefore a range of possible dynamic response amplitudes.

This paper presents numerical results coming from the computation of a shrouded blade's nonlinear dynamic response and comparison with experimental results. The numerical results are evaluated at the shroud contact interface and at locations coinciding with the measured locations. The objective of the calculation was to evaluate the performance curve, relating the response amplitude with the level of excitation force. In general, friction damped systems have performance curves that follow a predetermined pattern, as shown in [15]. For low excitations, the amplitude of the response grows quasi-linearly with the amplitude of the forcing (stick regime). For excitations that exceed a certain limit, the friction damping becomes predominant (gross slip regime) with respect to other damping sources, i.e., material damping and other unaccounted friction

damping sources (blade roots). Here, the amplitude stabilizes on a plateau value that remains quasi constant for increasing levels of excitation. This region of the performance curve identifies the amplitudes whereby the shroud is actively dissipating energy through friction. The response here is termed the “damped limit response” and is first evaluated numerically together with its level of uncertainty caused by the variability of the contact parameters and the non-uniqueness of the solution.

Available engine measurement data, taken from a range of load conditions, is then evaluated. Both tip timing and strain gauge data are available. The tip timing data is taken as the reference measurement for comparison with the numerical results and is used to verify the kinematic behavior as close as possible to the shroud contact location. The tip timing measurement results are presented and verified against strain gauge measurements, and then further evaluated for varying levels of aero excitation. The results are discussed in relation to the numerically calculated performance curve.

In detail, the paper is organized as follows. The bladed disk numerical model and contact model are presented in section 2. Section 3 provides the relevant features of the methodology followed to solve the nonlinear equilibrium equations, using the performance curve as a basis for all results. A sensitivity analysis evaluates the dependence of the obtained performance curves (with a special reference to the plateau region, or damped limit response) on the choice of the contact parameter values and contact conditions. Section 4 presents the numerical results for the best fit configuration of the model. The experimental set up and measurement verification are described in section 5, while section 6 discusses the comparison of experimental and numerical results.

2. NUMERICAL MODEL

A finite element (FE) model of a disk sector with shrouded blades, as shown in Figure 1, is reduced with the Craig Bampton Component Mode Synthesis (CB-CMS) technique. This reduction procedure allows to retain, as masters, both modal and physical degrees of freedom (d.o.f.). In this case, 100 modal d.o.f. have been chosen as master to ensure a high level of accuracy. The master physical d.o.f. are selected on the contact surfaces of the shroud and at some specific points on the blade airfoil where the displacement is measured (e.g., tip timing location) or where the excitation force is applied. A friction contact model is applied to the coincident nodes of the shroud contact interface.

The friction contact model, originally developed in [1] and [5] for the single HBM and then extended in [6] for the multi-harmonic balance method (MHBM), is capable of taking into account variations of normal load and contact point lift-off.

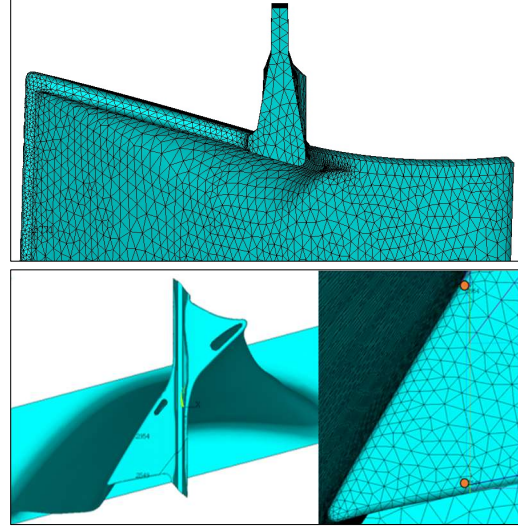


FIGURE 1: SOLID MODEL OF THE BLADE WITH SHROUD GEOMETRY (TOP) AND TIP TIMING MEASUREMENT LOCATIONS (BOTTOM).

According to this model, shown in Figure 2, the tangential and normal contact stiffnesses are modelled by springs of stiffness k_t and k_n respectively. A coefficient of friction μ is assumed between the contact surfaces.

The relative displacements in the tangential and normal directions are $u(t)$ and $v(t)$ respectively, while the amount of tangential slip between the contact surfaces is $w(t)$.

The normal contact force $N(t)$ is defined as

$$N = \max(N_0 + k_n \cdot v, 0) \quad (1)$$

where N_0 is the static normal load. If N_0 is positive, the bodies are in contact before vibration starts, while if N_0 is negative an initial gap exists between the two bodies. According to the value of the normal relative displacement, $v(t)$, three conditions are possible: full contact, partial lift-off, and full lift-off. If lift-off occurs, the normal contact load is set equal to 0, since negative values are not acceptable.

$$T = \begin{cases} k_t \cdot (u - w) & \text{stick} \\ \text{sgn}(\dot{w}) \cdot \mu \cdot N & \text{slip} \\ 0 & \text{lift-off} \end{cases} \quad (2)$$

Stick, slip and lift-off may alternate between each other during the periodic vibration. The effect of the variable normal contact load $N(t)$ on the hysteresis cycle of tangential contact load $T(t)$ is shown in Figure 2 (right).

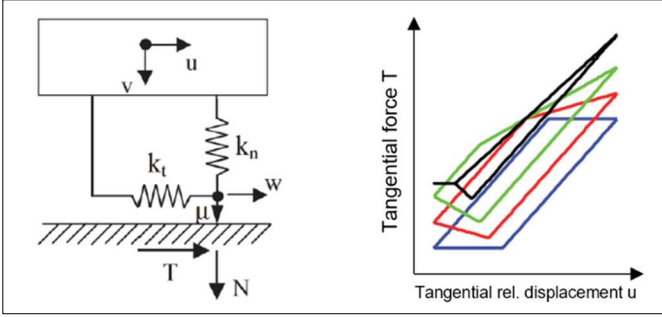


FIGURE 2: 1D RELATIVE DISPLACEMENTS AND VARIABLE NORMAL LOAD N : CONTACT MODEL (LEFT) AND TYPICAL HYSTERESIS CYCLES (RIGHT). BLUE (CONSTANT μ), RED AND GREEN (VARIABLE μ), BLACK (VARIABLE μ WITH PARTIAL LOSS OF CONTACT)

The contact model described above is fit to represent 1D tangential relative displacements. However, 2D tangential relative displacements of the contact points occur and modeling this contact assuming a linear trajectory can lead to an underestimation of the friction damping [7], [16]. In order to model this feature, two 1D contact elements like the one described above, are placed orthogonally to each other, in order to take into account the 2D trajectory of the contact points on the contact plane.

The disk sector is assumed to be rigid, i.e., no cyclic symmetry constraints are imposed. This significantly simplifies the procedure to obtain the CB-CMS reduced matrices without a significant loss of accuracy. It was in fact proved that, in this case, the disk has a very limited influence on the resonances under study (changes of 0.2%). Cyclic symmetry will instead be applied at the shroud location by imposing the cyclic symmetry conditions to the displacements between adjacent sectors.

2.1 Definition of the static normal preload and master contact nodes selection

The contact pressure distribution is obtained by running an Ansys static calculation with friction contact modeled using the Augmented Lagrange Contact formulation at the shroud interface. The static calculation includes nonlinear geometry and cyclic constraints at an offset from the shroud contact face. Centrifugal, thermal and pressure loads are included.

The result is a pressure distribution diagram shown in the left portion of Figure 3. This information needs to be transferred in terms of normal preload to each pair of master contact nodes. The contact node pairing may be complicated by non-coincident contact nodes on the two contact surfaces. FRIDA (FRiction DAMping) uses, as a starting point for its calculation, the position of the contact nodes after the static step. Therefore, even if one were to start from coincident meshes at the two contact surfaces, the final position of the contact nodes would be modified by the application of the centrifugal load and thermal boundary conditions within the static step. To handle this issue, a state-of-the-art interpolation technique like the one described in [17] is applied.

Before proceeding, it is necessary to define the contact node pair configuration. Two different configurations will be analyzed throughout the paper, both are shown in Figure 3.

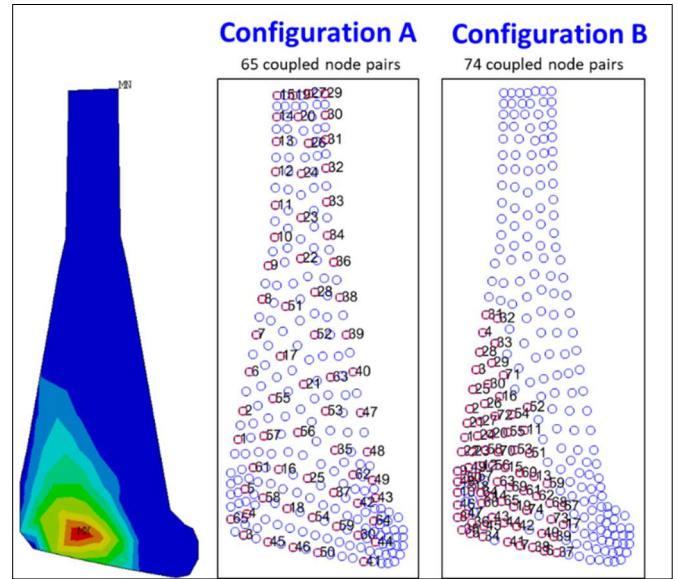


FIGURE 3: (LEFT) CONTACT PRESSURE DISTRIBUTION ON THE SHROUD SURFACE COMING FROM THE STATIC ANSYS CALCULATION. THE COLOR SCALE GOES FROM BLUE (LOW PRESSURE) TO RED (HIGH PRESSURE). (RIGHT) TWO DIFFERENT NODE PAIR SELECTIONS

The algorithm used to define the preload can be summarized as follows:

- the starting point is the pressure distribution shown in Figure 3 (left). The user will identify several subregions (here termed sr) inside the contact area and estimate their area A_i .
- start off with tentative values of $p_i = p_1, \dots, p_{sr}$, where p_i represents the i -th subregion mean pressure value, which should be in the range of values indicated in the Ansys calculation.
- compute the corresponding values of $N_i = N_1, \dots, N_{sr}$ using $N_i = p_i \cdot A_i$, that is the total load acting on each subregion.
- verify the equation $\sum_{i=1}^{sr} N_i = N$, where N is the total normal load acting on the contact surface and is an output of the Ansys calculation.
- if the equation above is verified, compute the normal contact load on each node pair in each subregion i : $\bar{N}_i = \frac{N_i}{n_i}$ where n_i is the number of node pairs in region i .
- if the equation above is not verified, modify values of p_i always remaining within the boundaries set by Ansys.

The algorithm allows the user to select only a subset of the nodes belonging to the contact area defined in Ansys, while still maintaining values of contact pressure coherent with those coming from the Ansys static calculation.

The \bar{N}_i values depend on the selection of contact node pairs. The authors investigated two possible contact configurations. In Configuration A, the chosen nodes are uniformly distributed over

the contact area. Given the pressure distribution shown in Figure 3, most nodes are loaded by a very low \bar{N}_i value. Choosing such a large number of contact node pairs from a low contact pressure subregion may therefore lead to an overestimation of the predicted dissipation, as a large number of contact node pairs will easily reach the slip condition. Furthermore, it may simulate contact conditions far from those truly encountered, i.e., forcing a contact where there is a gap.

Therefore, it was decided to also explore a different contact node pair configuration, Configuration B, as shown in Figure 3. In it, most of the contact nodes are selected from regions where the contact pressure is above a certain threshold. Based on the authors' experience on different friction damping devices for turbine blades (i.e., underplatform dampers, shrouds, snubbers, blade roots), the threshold can be set at 10% of the average contact pressure. The node selection of Configuration B is not only comparable with the contact status predicted by the Ansys static step, but it is also in line with service experience in terms of contact wear. The procedure to determine the preload at each contact node is the same as for Configuration A.

2.2 Selection of the contact parameters

The input parameters of the contact model of Figure 2 are the tangential and normal contact stiffness (k_t , and k_n), and the friction coefficient μ . Each node belonging to a node pair, is connected to the corresponding node on the other surface through one normal spring, here termed k_n^* , and two perpendicular tangential springs, here termed k_t^* . To choose representative values of these parameters, a sensitivity analysis has been performed on the full stick frequency. The full stick condition is here chosen as a reference for the contact stiffness sensitivity analysis because it is the contact status that maximizes the influence of k_t and k_n on the response, i.e., no loss of stiffness due to partial slip. Furthermore, the full stick condition is the contact status predicted by the Ansys static step. The results are shown in Figure 4 for a given mode. Similar trends are obtained for the remaining modes. The contact springs values shown in Figure 4 refer to the whole contact surface. It is here assumed that the contact stiffness is evenly shared among all n node pairs, therefore it holds:

$$k_n^* = \frac{k_n}{n}$$

$$k_t^* = \frac{k_t}{n}$$

It can be seen how the eigenfrequency is influenced by the value of contact springs. It can also be seen that above a given k_t and k_n threshold, a plateau is reached. Here, no significant frequency increase is observed, even for significant increases in contact stiffness values.

It was then chosen to select the smallest possible value of contact stiffness that produces eigenfrequencies as close as possible to the Ansys reference. In this case the resulting values are of the order of $k_n = k_t = 10^9$ N/mm.

The friction coefficient was set at 0.4, and is a value derived from experiments at the same temperature expected at the shroud location and further confirmed by recent experimental tests [18]. The choice of the contact parameters and contact node pairs will be further analyzed in the next section. Here, a sensitivity analysis is shown to assess how the amplitude of the forced blade response is influenced.

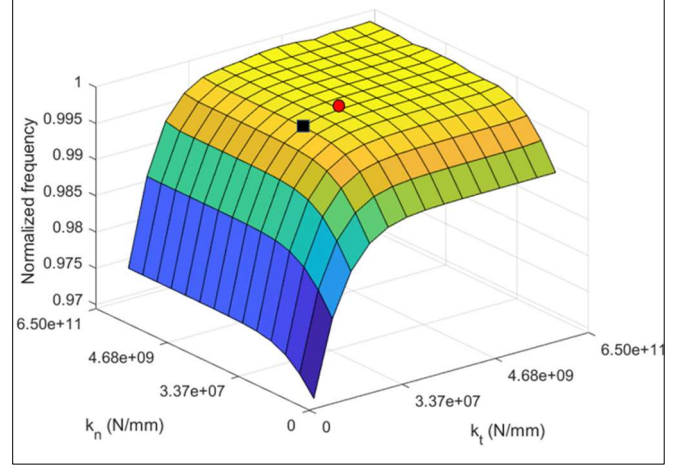


FIGURE 4: EFFECT OF THE VARIATION OF THE NORMAL AND TANGENTIAL CONTACT SPRINGS ON THE FREQUENCY CHOSEN AS REFERENCE. THE RED DOT REPRESENTS THE CONTACT STIFFNESS CHOICE USED TO PRODUCE THE RESULTS IN FIGURE 5, THE BLACK SQUARE WILL BE USED TO CARRY OUT THE SENSITIVITY ANALYSIS IN FIGURE 7.

3. NON-LINEAR FORCED RESPONSE

The governing equation of motion of a discrete dynamic system subjected to local nonlinearity in the contact area makes the time-domain solution of the equilibrium equations prohibitive. Since the steady state part of the solution is of interest, the equations are re-written in the frequency domain using the well-known MHBM [10]:

$$(-(h\omega)^2 M + i(h\omega)C + K)X^h = F_E^h + F_C^h \quad (1)$$

Where h is the harmonic index, X is the vector of displacements in the frequency domain, M , C and K are the mass, damping and stiffness matrices respectively, F_E is the vector of external excitation and F_C is the vector of contact forces which, in turn, depends on displacement.

The numerical tool FRIDA (FRiction DAMping) iteratively solves Eq. (1) by minimizing the residual:

$$R^h = (-h\omega)^2 M + i(h\omega)C + K)X^h - F_E^h - F_C^h \quad (1)$$

A Newton-Raphson algorithm is used. The initial guess on the displacement vector X^h is adjusted as a function of the excitation level with a purposely developed technique to speed the convergence rate. In it, the initial guess on the displacement vector is computed as the solution of a linear system where the node-to-node contact element is substituted by a simple set of

linear springs, whose constants take different values to approximate different contact states (i.e., k_n and k_t for the stick case, lower values to include different percentages of gross slip and lift-off). This technique uses, in a different context, a similar methodology to that presented in [3] to define a reduction basis. The vector of contact forces is obtained by applying the contact model described in section 2 through the Alternating Frequency Time procedure [19]. Other state-of-the-art features, like the exact condensation procedure [19] and [20], where linear d.o.f. are expressed as a function of the nonlinear d.o.f. are implemented to reduce the computational effort.

FRIDA is used to compute the Frequency Response Function in terms of displacements at key locations on the blade airfoil where master nodes from the CB-CMS reduction have been selected. The nodes correspond to the locations of the tip timing displacement measurements and will be later used for the experimental numerical comparison (see section 5). The evaluation is performed for increasing values of the excitation level $|F_E^1|$. The excitation is here obtained using a mono-harmonic proof excitation force to inject energy in the system. The amplitude of $|F_E^1|$ is gradually increased to trigger different levels of nonlinearity at the contact (i.e. from full stick to gross slip/lift-off).

For each excitation level, the FRF is computed for a series of discrete frequency steps, centered around the expected resonance frequency. The resonance condition is identified by picking the frequency step associated with the maximum amplitude. Figure 5 shows the normalized displacement amplitude and resonance frequency as a function of the excitation level for Configuration A. The excitation level is normalized by a reference value of the proof excitation force $|F_{E,ref}^1|$, which is kept constant throughout the paper, i.e., all diagrams shown as a function of the normalized force $|F_E^1|/|F_{E,ref}^1|$ use the same scale and can therefore be directly compared. The value of $|F_{E,ref}^1|$ is chosen as the minimum excitation level which ensures that a sufficient level of contact points have reached the slip condition. As a result, for $|F_E^1|/|F_{E,ref}^1| \geq 1$ the maximum response settles on a stable plateau. This value was found to be approximately the same for both Configuration A and B.

The reader will notice that response and frequency performance curves, depending on the excitation level, may display non unique values. In fact, Figure 5 shows the maximum and the minimum encountered results. This is because the solution is not unique whenever the contact conditions transition from full stick to a mix of stick/slip/lift-off. In fact, a unique curve is visible for the first few explored normalized force values ($|F_E^1|/|F_{E,ref}^1| < 0.3$), as for limited excitation levels, most contact points remain in the full stick condition.

The multiplicity of the solution comes from the fact that there exists a coupling between the static and the harmonic components of the vector of displacements. As demonstrated in [20], different vectors of displacement, corresponding to different contact conditions, can satisfy the same set of equilibrium equations, with all other parameters being equal

(external forces, contact parameters values, contact node selection, etc.).

This phenomenon has already been encountered both numerically and experimentally in different friction damped systems [13] and [14] and will be discussed further in section 4. Here, a brief description of the strategy proposed by the authors to explore the min-max envelope of the performance curve is offered.

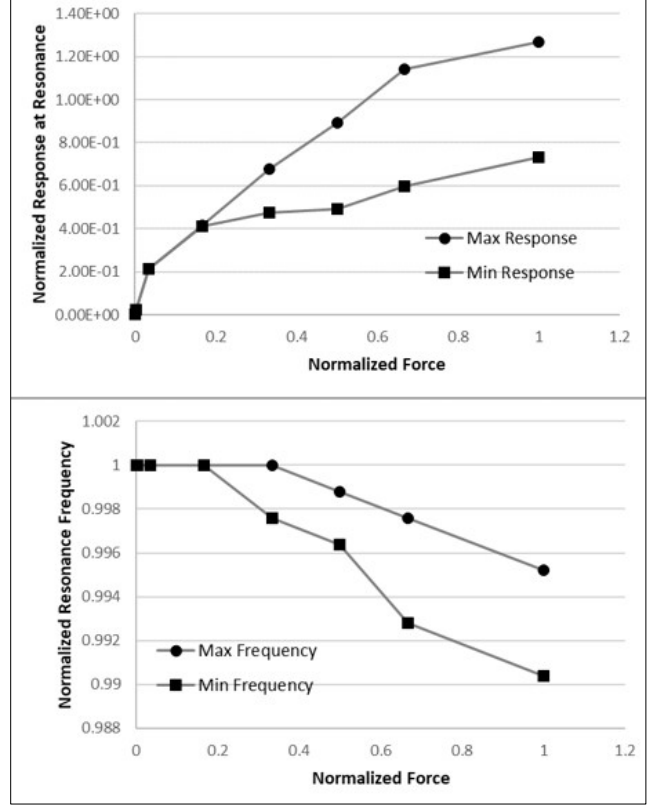


FIGURE 5: PERFORMANCE CURVES IN TERMS OF MAXIMUM DISPLACEMENT AT TIP TIMING LOCATION (TOP) AND RESONANCE FREQUENCY (BOTTOM) FOR COUPLED SHROUD CONFIGURATION A.

To trigger the appearance of multiple solutions, several strategies can be adopted [14]. The one devised by the authors and applied in the present work is to feed the solver with different initial guesses on the vector of displacements, using the ad-hoc technique described above. Each of these different initial guesses are tailored to represent a different set of contact states on the contact node pairs. Despite the subsequent necessary modifications operated by the solver to find an accurate solution, it has been observed that there exists a strong correlation between the contact conditions assumed during the creation of the initial guess and the final contact conditions of the converged solution. Thus, impacting the numerically evaluated response amplitude. For each excitation level, a Latin Hypercube Sampling procedure is performed to define a set of different initial guesses on the vector of displacements. A total of 100 samples were tested for each excitation level, although it has been observed that the same min-max envelope can be obtained with a smaller set of properly

chosen samples. Given the numerosity of the samples, the authors are confident that the min-max envelope of the performance curve is well represented.

Given the unavoidable uncertainty on the chosen contact parameters and contact nodes selection, the following subsections perform a sensitivity analysis to show the impact that variations of the different parameters and modeling choices have on the performance curves.

3.1 Influence of contact parameter values

The first sensitivity analysis to be performed is on the friction coefficient value, which is here allowed to vary within the [0.3-0.5] range. Increasing the friction coefficient expands the initial quasi-linear trend, as contact nodes will need a larger excitation level to reach the gross slip condition. Predicting the influence of the friction coefficient for larger excitation levels is not as easy. In the case shown in Figure 6, a smaller friction coefficient leads to smaller displacement amplitudes for large force levels. This is because more contact nodes reach gross slip and/or nodes slip for a longer portion of the period of vibration, thus increasing the dissipated energy.

By looking at the three curves in Figure 6, it can be concluded that variations of friction coefficient have a moderate effect on the final mean response levels ($\pm 7\%$).

As part of the present sensitivity analysis, the contact stiffness values were changed, always remaining within the plateau region. In detail, the tangential contact stiffness k_t is reduced by three orders of magnitude (see black square in Figure 4). This choice is motivated by the authors' experience on measured contact stiffness values [22], where encountered k_t values are typically lower than k_n values. This strategy ensures a lower slip rate (i.e., reduced dissipated energy), as larger displacements are needed to arrive to the friction force limit, with all other parameters being equal. The resulting curve is shown in Figure 7. The trend is the expected one (lower k_t values lead to a lower dissipated energy and larger displacements), however, despite the large variation of k_t , the influence is still moderate ($\pm 5\%$).

To conclude, variations of the contact parameters within a reasonable range have moderate effect on the performance curves, i.e., the uncertainty introduced by the solution multiplicity is significantly larger. For this reason, the initial values identified in section 2 are maintained for the final experimental and numerical comparison. It should be noted that the same set of sensitivity analyses were repeated for Configuration B yielding similar results and is therefore here not shown for brevity.

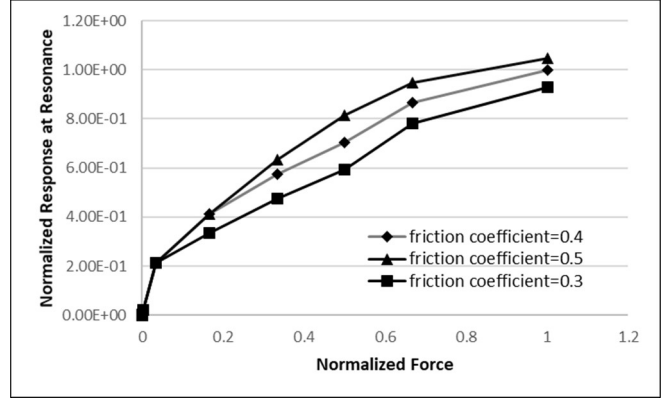


FIGURE 6: INFLUENCE OF THE FRICTION COEFFICIENT ON THE RESPONSE PERFORMANCE CURVE (MEAN VALUES)

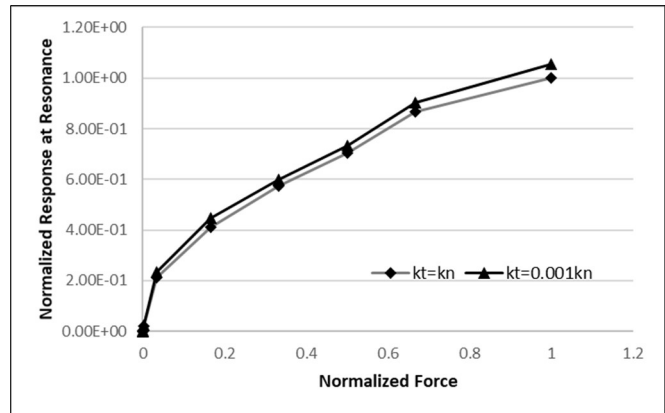


FIGURE 7: INFLUENCE OF THE CONTACT STIFFNESS VALUES ON THE RESPONSE PERFORMANCE CURVE (MEAN VALUES).

3.2 Influence of the contact surface selection

This section investigates the influence of the selected contact surface area on the calculated performance curve. The comparison between the performance curves obtained for Configuration A, and the one obtained for Configuration B is shown in Figure 8. As expected, the response multiplicity is encountered in both cases, especially for larger excitation levels. The reader will notice that the Configuration B results are generally higher, especially the maximum response envelope (+30%). This is most likely due to the fact that Configuration A is enforcing the contact in a low contact pressure region, thus artificially reducing the overall mobility of the shroud. The nodes selected for Configuration B, on the other hand, all come from a restricted area with higher contact pressure. This increases both the mobility of the shroud (and consequently the tip displacements) and potentially reduces the amount of dissipation, as the nodes have generally a higher assigned preload when compared with those from Configuration A.

A preliminary comparison of the numerical displacements with the tip timing results confirmed that the results coming from Configuration B are more consistent with the experimental observations. Therefore, it was decided to perform a complete and thorough investigation of the performance curve for Configuration B. The results are shown in the next section.

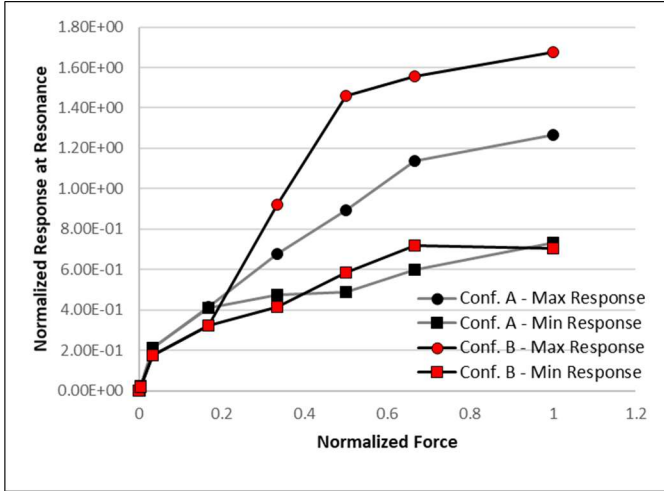


FIGURE 8: INFLUENCE OF THE CONTACT NODES SELECTION ON THE RESPONSE PERFORMANCE CURVE.

4. FORCED RESPONSE RESULTS FOR THE SELECTED CONFIGURATION

A final check for Configuration B is performed to confirm that with the selected contact parameters and contact area, the shroud deformation is adequately represented by the FRIDA reduced model. To do this, the “stuck” shroud contact condition with selected contact stiffness values from section 3.1 is evaluated. The shroud axial and circumferential deformation are calculated for the linear case at the prescribed tip timing location on the shroud for a complete vibration cycle. This is also evaluated for the Ansys FE linear model, providing modal shroud deformation at the same location for the given mode. A scale factor is derived from the ratio of the FRIDA and Ansys Vertex (in axial direction) on the shroud elliptical trajectory and is then further applied to the Ansys modal deformation over the complete vibration cycle. The FRIDA and scaled Ansys modal axial and circumferential deformations are presented in Figure 9. A good match is shown qualitatively, and it is concluded that the FRIDA reduced model, together with stiffness coefficients represent the shroud stiffness and mobility given in the Ansys linear full model.

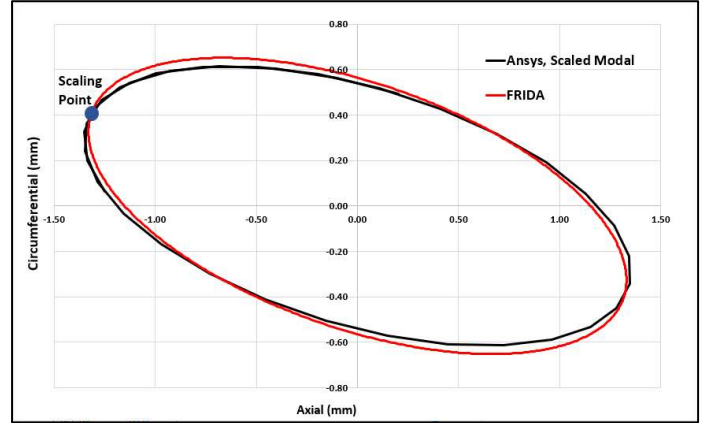


FIGURE 9: ANSYS-FRIDA COMPARISON OF BLADE TIP TRAJECTORY FOR THE CHOSEN CONTACT PARAMETERS AND CONTACT CONFIGURATION IN THE FULLY STUCK LINEAR CASE

Figure 10 shows the response performance curve obtained for Configuration B, with the nominal values of contact parameters defined in section 2. This is judged as the best configuration fit for the experimental-numerical comparison of section 6.

The reader will notice that in this case the response is not normalized, rather the numerical equivalent of the tip timing displacement is shown, in preparation for the experimental numerical comparison. Also, the investigated excitation level has now been extended to $|F_E^1|/|F_{E,ref}^1| = 2$, verifying the plateau region for the response level of $|F_E^1|/|F_{E,ref}^1| \geq 1$. Here, the shroud is actively dissipating energy through friction.

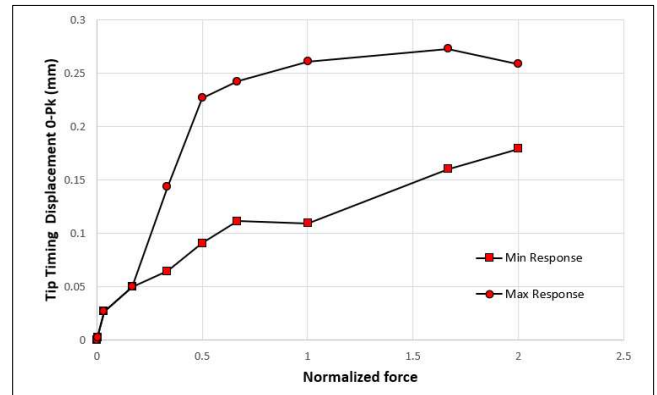


FIGURE 10: PERFORMANCE CURVES IN TERMS OF MAXIMUM DISPLACEMENT AT TIP TIMING LOCATION

Figure 11 is here used to further investigate the cause of the multiple solutions. Figure 11 shows histograms, where the height of the bars, normalized at 1, represents the total time duration for a period of vibration. A total of 74 different bars represents each contact node pair. The color code represents which time % of the period is spent in the three possible contact states: blue for stick, red for slip and yellow for lift-off. The sum of the three contributions will be in all cases equal to 1, but different contact nodes will display different states.

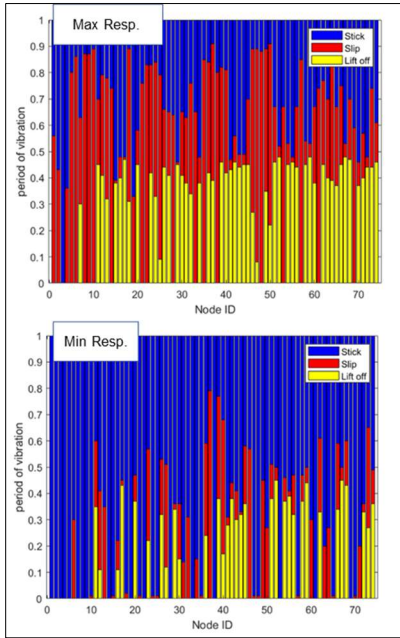


FIGURE 11: HISTOGRAM PLOTS REPRESENTING THE CONTACT STATE AT THE DIFFERENT NODE PAIRS FOR NORMALIZED FORCE=1 FROM FIGURE 10 - MAX AND MIN RESPONSE.

The comparison between the maximum and minimum response at unitary normalized force $|F_E^1|/|F_{E,ref}^1| = 1$ proves that the different solutions originate from a different contact pattern.

5. EXPERIMENTAL TESTS

Verification of the numerical model was carried out using available engine test data taken from a range of load conditions. Both tip timing and strain gauge measurement systems were available. High temperature strain gauges were applied at airfoil and shank locations to measure and characterise the individual blade behaviour. In parallel, six tip timing probes, schematically shown in Figure 12, were assembled, and loaded down on the inner casing to measure the all-blade system response.

The tip timing probes were purged, cooled, and lensed probes loaded down on the inner casing with a view on the shroud. The timing data was acquired by an Agilis Data Acquisition System, using the time of arrival from the shroud edge crossing. Selected blades were marked with white reflective marker to verify the blade positions for future comparison.

The strain gauge measurement chain included high temperature quarter bridge strain gauges with MI (mineral insulated) cables attached to the rotor and routed to a high temperature telemetry system mounted at the turbine shaft end. National Instruments PXI 4496 dynamic acquisition cards were used for acquisition together with Corvus analysis software, a multi process distributed dynamic acquisition system.

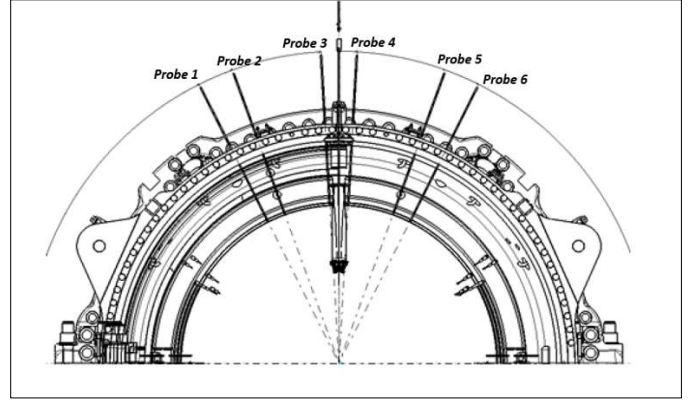


FIGURE 12: SCHEMATIC VIEW OF THE INSTALLED TIP TIMING PROBES IN THE CASING.

5.1 Measurement Verification

The tip timing data was taken as the reference system for comparison with the numerical results since the complete bladed system can be characterised with this measurement and it is the tip movement that drives the friction damping at the shroud contact faces.

Prior to doing this, a verification of the tip timing measurement results against available strain gauge measurements was carried out to ensure consistency and reliability in the measurement. This section presents the results coming from this verification, comparing both frequency results and consistent transfer factors between both data sets.

As a first step, the frequency measured by both systems were overlaid and compared. The results are shown in Figure 13, providing the all-blade tip timing Travelling Wave results together with the individual blade Strain Gauge FFT results at selected time points. The top plot provides an overlay of the tip timing frequency results for each measured nodal diameter (ND) component together with the strain gauge FFT frequency result at selected time instances. The bottom left-hand plot presents an individual blade strain gauge spectrum plot, illustrating the same ND components shown to be present in the selected blade's response. Finally, the bottom right-hand plot provides an overlay of a strain gauge linear average FFT for a selected short time interval. Here, all data coming from the instrumented blades are overlaid. A good match between both measurement systems in terms of measured frequency and the ND content was concluded.

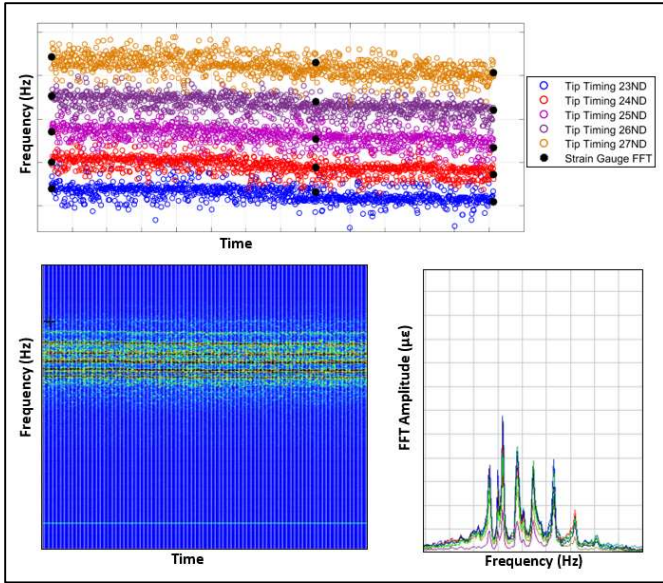


FIGURE 13: TOP PLOT: OVERLAY OF TIP TIMING & STRAIN GAUGE FREQUENCY MEASUREMENTS; BOTTOM LEFT: STRAIN GAUGE SPECTRUM PLOT; BOTTOM RIGHT: STRAIN GAUGE FFT

The strain gauge data was again used as a reference to attempt to verify the consistency and quality of the tip timing amplitude measurements.

The dynamic strain measurement was postprocessed with a Butterworth bandpass filter defined about the evaluated frequency range of the group of nodal diameters shown in the strain gauge spectrum plot and FFT plot in Figure 13. A Time Window of 38ms length was used, from which the 0-Pk amplitude was recorded. The tip timing data was processed using a 5 data point curve fit for each blade passing, utilising 5 of the installed probes. The calculated frequencies resulting from the traveling wave analysis were used to set up the curve fit. The 0-Pk Amplitudes were recorded at a time increment of 16ms. In essence, both approaches utilise a frequency filter approach based upon an initial evaluation of the frequency content of the data. However, the strain gauge result provides a peak amplitude result over several continuous vibration cycles, whilst the tip timing result provides the peak amplitude over one vibration cycle event per revolution. Additional challenges occur due to the ND content. Superimposed, the multiple ND content results in a modulated time signal in amplitude, as shown in Figure 14. Here, a frequency bandwidth filtered time function is shown for three selected airfoil strain gauges, presenting the continuous amplitude variation within a given time window. Capturing this response with a 1/rev curve fit event would inevitably result in a loss of data. Therefore, it was important to evaluate and compare this data with a statistical view in mind.

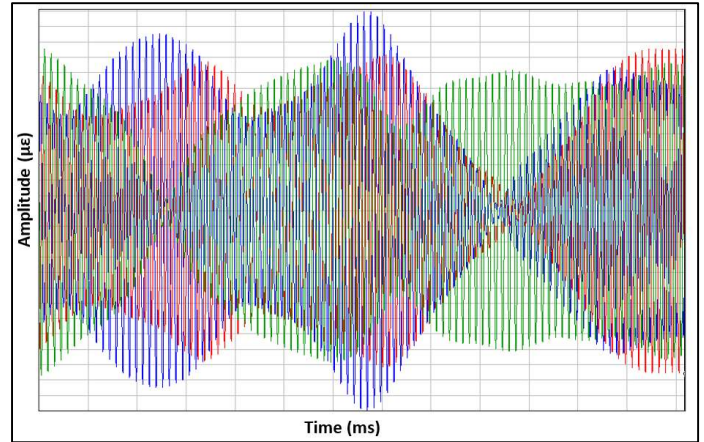


FIGURE 14: STRAIN GAUGE BANDPASS FILTERED TIME SIGNAL FROM THREE INSTRUMENTED BLADES.

Data sets taken from two separate test runs, test 1 and test 2, were evaluated using the moving average and transfer function between both data sets. The moving average was used to minimise the influence of the additive and subtractive noise present in both measurement systems, and to statistically account for the differing sampling approaches of the signal shown in Figure 14. The airfoil gauge close to the shroud is selected for comparison. An overlay of the data is shown in Figure 15 (test 2) and Figure 16 (test 1), where the strain gauge data is scaled to the tip timing data with a fixed transfer factor. It is visually clear from both test data that, as the measurement supersedes the tip timing noise floor of 0.05mm 0-Pk, a good correlation of tip timing and strain gauge is shown. This is especially apparent when viewing the lower plot in each of the figures, where the timeline is extended with a range of response scenarios.

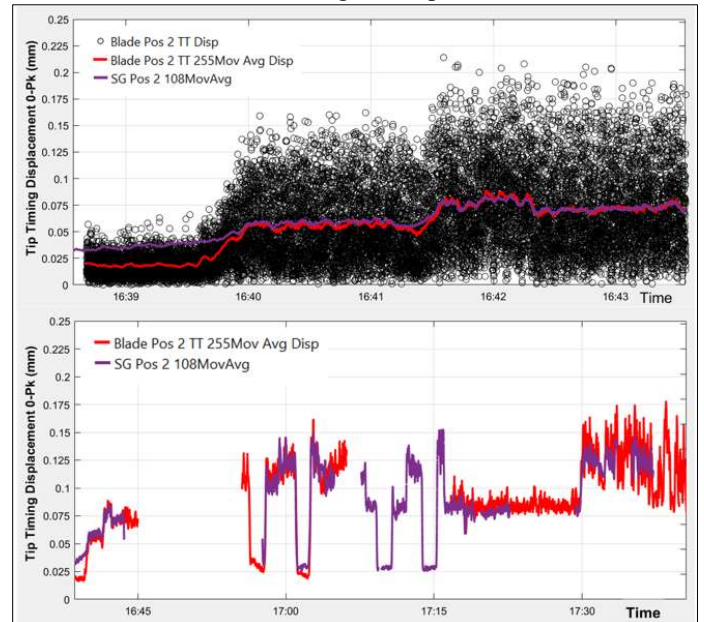


FIGURE 15: TEST 2, OVERLAY OF TIP TIMING (TT) AND SCALED STRAIN GAUGE (SG) MOVING AVERAGE RESULTS.

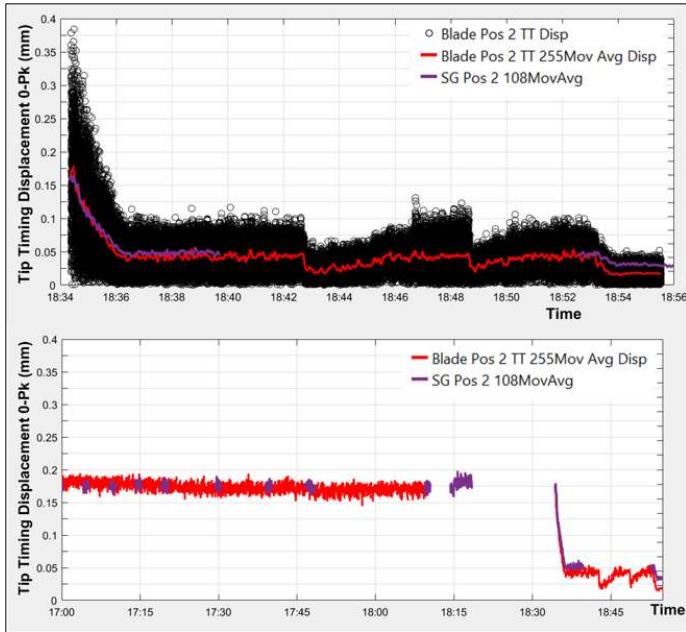


FIGURE 16: TEST 1, OVERLAY OF TIP TIMING (TT) AND SCALED STRAIN GAUGE (SG) MOVING AVERAGE RESULTS.

A portion of the highest responding amplitudes from test 2 were sampled and the event distribution calculated. The strain gauge data was scaled using the evaluated transfer factor based on the overlay of the moving averages. The result is shown in Figure 17. It is clear from the results that there is a very reasonable comparison of the tip timing and strain gauge distribution. The main differences are shown at the extremities of the measured amplitudes, within the tip timing noise floor and the rare higher displacement peak events. This is mainly attributed to the independent sources of noise and different data (filtered) processing strategies.

In general, it is found that above the evaluated noise floor of 0.05mm 0-Pk, the tip timing provides a robust measurement which transfers well and consistently to the strain gauge data. This is particularly the case when the moving average result is considered.

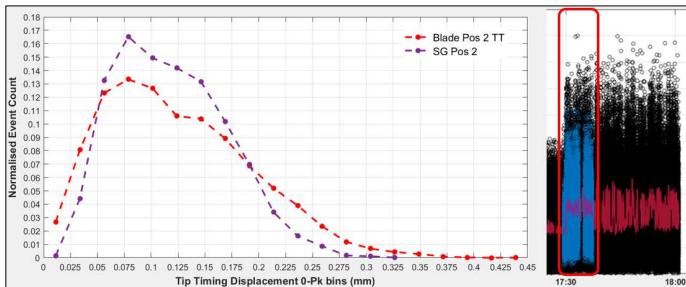


FIGURE 17: TEST 2, EVENT DISTRIBUTION OF TIP TIMING (TT) DISPLACEMENT. STRAIN GAUGE (SG) RESULTS ARE TRANSFERRED TO TIP TIMING DISPLACEMENT USING EVALUATED TRANSFER FACTOR.

6. NUMERICAL-EXPERIMENTAL COMPARISON

Using the data processing approach described in section 5, the all-blade measurement was evaluated for test 2. The plot in Figure 18 presents tip timing moving average response amplitudes versus a scaled aero excitation trend derived from measured engine parameters. The shown aero excitation trace is intended to provide the trend of forcing rather than absolute values. Therefore, no numerical scale is provided for this. The minimum and maximum tip timing trends represent data coming from the minimum and maximum responding blades respectively.

In general, it is seen qualitatively that the measured amplitudes follow the aero excitation trend in a linear manner. This behavior appears to deviate later in time when the aero excitation increases from Level 1 to Level 2 and then further to Level 3.

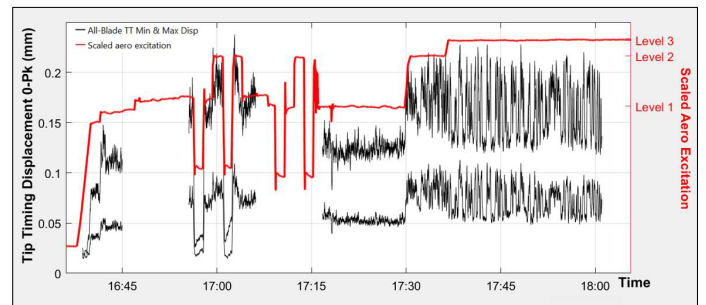


FIGURE 18: TEST 2, MINIMUM AND MAXIMUM TIP TIMING (TT) MOVING AVERAGE DISPLACEMENT VERSUS SCALED AERO-EXCITATION.

The forementioned three levels of aero excitation, level 1, level 2, and level 3 are shown in more detail in Figure 19, Figure 20, and Figure 21.

In Figure 19, the all-blade tip displacement results are shown to sit within a band of 0.05mm 0-Pk to 0.15mm 0-Pk. The overall behaviour shows very little variation with constant level 1 aero excitation. As the aero excitation is increased within this plot, an increase in tip movement is observed, in addition to an increased fluctuation of the response.

This is markedly shown in Figure 20. Here, the all-blade system exhibits a more cyclic response within a range of 0.07mm 0-Pk to 0.23mm 0-Pk. The aero excitation remains constant at level 2. The all-blade measured tip displacement is shown in Figure 21 for a further increase of aero excitation to level 3. The cyclic amplitude growth and reduction here is more pronounced but maintaining around the same amplitude range of 0.05mm 0-Pk to 0.24mm 0-Pk. This cyclic response amplitude behaviour is clearly indicative of a nonlinear friction damped system.

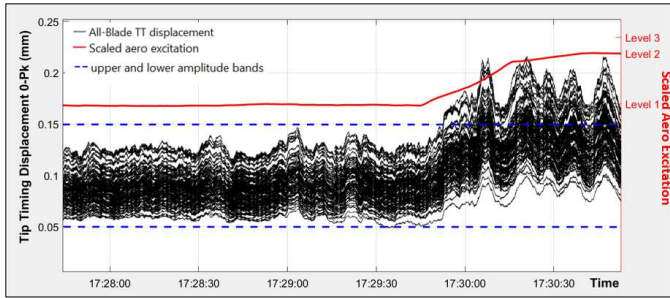


FIGURE 19: TEST 2, ALL-BLADE TIP TIMING (TT) MOVING AVERAGE DISPLACEMENT AT LEVEL 1 AERO EXCITATION.

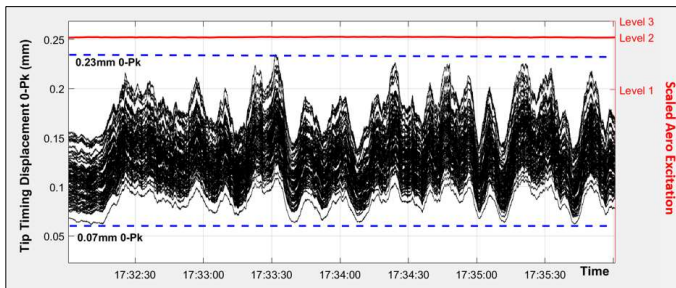


FIGURE 20: TEST 2, ALL-BLADE TIP TIMING (TT) MOVING AVERAGE DISPLACEMENT AT LEVEL 2 AERO EXCITATION.

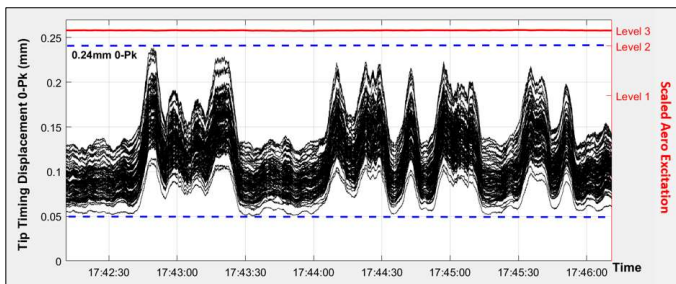


FIGURE 21: TEST 2, ALL-BLADE TIP TIMING (TT) MOVING AVERAGE DISPLACEMENT AT LEVEL 3 AERO EXCITATION.

The FRIDA numerical results, taken from Figure 10 in section 4 are shown again below in Figure 22, with a focus on the effective damping region of the performance curve, i.e., damped limit response or plateau region. Upon evaluation of the upper trace of the performance curve, it is shown that effective damping is predicted to initiate at around 0.23mm 0-Pk tip (tip timing) displacement. Evaluating the measured displacements from Figure 19, Figure 20 and Figure 21 shows a very good kinematic comparison with the numerical results. A clear limit response, in relation to the increasing aero force, is shown from the measurement at around 0.23mm 0-Pk and 0.24mm 0-Pk. Additionally, the exhibited cyclic amplitude behaviour with constant aero excitation further substantiates this limit response.

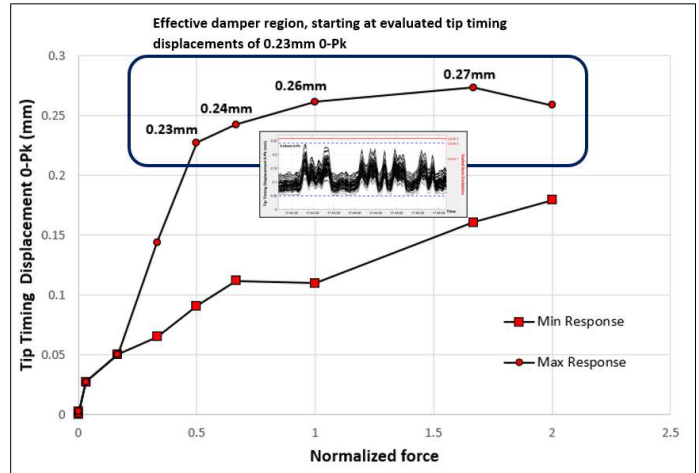


FIGURE 22: NUMERICAL PERFORMANCE CURVE TAKEN FROM FIGURE 10 WITH HIGHLIGHTED EFFECTIVE DAMPER REGION.

7. CONCLUSION

The numerical tool FRIDA is here used to compute the nonlinear response of a shrouded blade at different excitation levels, with a particular focus on the damped limit response, i.e., the blade response when the shroud is actively dissipating energy through friction. The influence of the contact parameters and selected contact nodes is analyzed through a sensitivity analysis and a best fit configuration is identified. The presence of multiple solutions originating from different possible stick and slip lift-off patterns at the contact is investigated and closely tracked. The numerical equivalent of tip timing displacement for a damped limit response is evaluated to compare with measurements coming from real engine test data.

Tip timing data from engine test is used as the reference measurement for comparison with the numerical results. The robustness and consistency of the data is verified against available strain gauge data as a first step. Subsequently, the measured tip displacement behavior in relation to aero excitation is evaluated and shown to present a clear limit response as excitation increases. Comparing measurement and calculation results, a strong correlation is found between calculated and measured limit response tip displacement for the given shroud contact configuration.

The reported results here show potential for using a numerical evaluated performance curve to evaluate the level of blade tip movement needed to produce a damped limit response for an actual engine scenario. This information, combined with knowledge of modal transfer functions, can be used to calculate the airfoil stress state, and would offer valuable information on the mechanical integrity of the blade under real operating conditions.

ACKNOWLEDGEMENTS

The authors would like to acknowledge the good collaboration with Ron Washburn, Agilis. The tip timing data coming from this collaboration was included in the paper.

An additional acknowledgement is given to the Ansaldo test team who organized and performed the engine tests referenced in this paper.

REFERENCES

- [1] Srinivasan A. V., “Flutter and Resonant Vibration Characteristics of Engine Blades”, *J. Eng. Gas Turbines Power*. 1997, vol. 119(4), pp. 742-775.
- [2] Herzog A., Krack M., Panning-von Scheidt L., Wallaschek J., “Comparison of Two Widely-Used Frequency-Time Domain Contact Models for the Vibration Simulation of Shrouded Turbine Blades”, *Proc. ASME Turbo Expo 2014*, GT2014-26226.
- [3] Gastaldi C., Zucca S., Epureanu B.I., “Jacobian projection reduced-order models for dynamic systems with contact nonlinearities”, *Mechanical Systems and Signal Processing*, 2018, vol. 100, pp. 550-569.
- [4] Schwarz S., Kohlmann L., Hartung A., Gross J., Scheel M., Krack M., “Validation of a Turbine Blade Component Test With Frictional Contacts by Phase-Locked-Loop and Force-Controlled Measurements”, *J. Eng. Gas Turbines Power*. 2020, vol. 142(5).
- [5] Yang B.D., Chu M. L., Menq C. H., “Stick–Slip–Separation Analysis and Non-Linear Stiffness and Damping Characterization of Friction Contacts Having Variable Normal Load”, *Journal of Sound and Vibrations*, 1998, vol. 210(4), pp. 461-481
- [6] Cardona, A., Coune, T., Lerusse, A., and Geradin, M., 1994, “A Multiharmonic Method for Nonlinear Vibration Analysis,” *Int. J. Numer. Methods Eng.*, 37(9), pp. 1593–1608
- [7] Firrone, C. M., and Zucca, S., 2011, *Modelling Friction Contacts in Structural Dynamics and Its Application to Turbine Bladed Disks*, Numerical Analysis—Theory and Application, Prof. Jan Awrejcewicz (ed.), InTech, Rijeka, Croatia, Ch. 14, pp. 301–334
- [8] Siewert, C., Panning, L., Wallaschek, J., and Richter, C., 2010, “Multiharmonic Forced Response Analysis of a Turbine Blading Coupled by Nonlinear Contact Forces,” *ASME J. Eng. Gas Turbines Power*, 132(8), p. 08250.
- [9] Petrov, E. P., and Ewins, D. J., Analytical Formulation of Friction Interface Elements for Analysis of Nonlinear Multi-Harmonic Vibrations of Bladed Disks, *ASME. J. Turbomach.* April 2003; 125(2): 364–371
- [10] M. Krack; J. Gross, *Harmonic Balance for Nonlinear Vibration Problems*, 2019, Springer.
- [11] Gastaldi C., Gola M.M., “Criteria for best performance of pre-optimized solid dampers”, *Proceedings of the ASME Turbo Expo 2018*, vol. 7C, GT2018-75961, doi: 10.1115/GT2018-75961.
- [12] Pesaresi L., Armand J., Schwingshackl C.W., Salles L., Wong C., An advanced underplatform damper modelling approach based on a microslip contact model, *Journal of Sound and Vibration*, 2018, vol. 143(1), pp.327-340.
- [13] C. Gastaldi, J. Gross, M. Scheel, T. M. Berruti, M. Krack, Modeling complex contact conditions and their effect on blade dynamics, *J. Eng. Gas Turbines Power*, vol. 143(1): 011007. <https://doi.org/10.1115/1.4049186>.
- [14] E. Ferhatoglu, S. Zucca, Determination of periodic response limits among multiple solutions for mechanical systems with wedge dampers, *J Sound Vib.* 494 (2021)115900, <https://doi.org/10.1016/j.jsv.2020.115900>
- [15] Cameron T. M., Griffin J. H., Kielb R. E., Hoosac T. M., “An Integrated Approach for Friction Damper Design”, *J. Vib. Acoust. Apr* 1990, vol. 112(2), pp. 175-182.
- [16] Griffin, J. H., and Menq, C. H., Friction Damping of Circular Motion and Its Application to Vibration Control, *ASME Journal of Vibration and Acoustics*, vol. 113, 1991, pp. 225–229.
- [17] Zucca S., Gola M.M., Piraccini F., “Non-Linear Dynamics of Steam Turbine Blades With Shroud: Numerical Analysis and Experiments”, *Proceedings of the ASME Turbo Expo 2012*, vol. 6, pp. 665-674, doi: 10.1115/GT2012-69692
- [18] Lavella M., Botto D., “Fretting Fatigue Analysis of Additively Manufactured Blade Root Made of Intermetallic Ti-48Al-2Cr-2Nb Alloy at High Temperature”, *Materials* 2018, 11(7), 1052.
- [19] Krack M., Salles L., Thouverez F., “Vibration Prediction of Bladed Disks Coupled by Friction Joints”, 2017, *Archives of Computational Methods in Engineering*.
- [20] M. Berthillier; C. Dupont; R. Mondal; J.J. Barrau, *Blades Forced Response Analysis with Friction Dampers*, 1998. *Journal of Vibration and Acoustics* 120(2), pp. 468–474.
- [21] Zucca S., Firrone C.M., “Nonlinear dynamics of mechanical systems with friction contacts: Coupled static and dynamic Multi-Harmonic Balance Method and multiple solutions”, 2014, *Journal of Sound and Vibration*, 333(3), pp. 916-926.
- [22] Gastaldi, C.; Gola, M. M., 2016. “Testing, simulating and understanding under-platform damper dynamics”. In *Proceedings of the VII European Congress on Computational Methods in Applied Sciences and Engineering (ECCOMAS Congress 2016)*.